

Homogeneous nucleation and droplet growth in supersaturated argon vapor: The cryogenic nucleation pulse chamber

Alexander Fladerer^{a)} and Reinhard Strey^{b)}

Institut für Physikalische Chemie, Universität zu Köln, Luxemburger Straße 116, D-50939 Köln, Germany

(Received 29 December 2005; accepted 20 February 2006; published online 27 April 2006)

We built a cryogenic nucleation pulse chamber for measuring homogeneous nucleation rates of argon. First measurements show that the growth rate of argon droplets at nucleation conditions is rather high so that nucleation and growth could not yet be decoupled. Nevertheless, the experiments permit an estimate of the onset of nucleation corresponding to a nucleation rate of $J = 10^{7(\pm 2)} \text{ cm}^{-3} \text{ s}^{-1}$ at temperatures $52 < T/K < 59$ and supersaturations around $S \approx 10$. Despite their preliminary nature these experiments indicate a severe failure of the classical nucleation theory, which predicts nucleation rates on the order of $10^{-28} - 10^{-13} \text{ cm}^{-3} \text{ s}^{-1}$ for the quoted conditions. Recent calculations based on density functional theory can only partially explain the discrepancy. In addition to the first nucleation experiments, we obtained and analyzed growth curves for argon droplets from constant angle Mie-light scattering. The good agreement of the experimental growth curves with model calculations according to Fuchs and Sutugin [*Highly Dispersed Aerosols* (Ann Arbor Science, Ann Arbor, MI, 1970)] permits a near-quantitative description of the experimental light-scattering signal. The procedure provides an estimate for the number density of the droplets along with a measure of their polydispersity. © 2006 American Institute of Physics.

[DOI: [10.1063/1.2186327](https://doi.org/10.1063/1.2186327)]

I. INTRODUCTION

Since the fundamental experiments of Wilson¹ (1897), homogeneous nucleation in supersaturated vapors has been studied with various devices and substances.² In general, only the onset conditions of nucleation depending on the sensitivity of the used experimental setup could be measured. In 1965 Allard and Kassner³ introduced the concept of nucleation pulses for measuring nucleation rates by decoupling nucleation and growth of droplets. Wagner and Strey further developed this principle constructing a nucleation pulse chamber which yields nucleation rates as a function of supersaturation at selectable constant temperature. The current state of the nucleation pulse chamber which underwent a number of improvement steps is described by Strey *et al.*⁴

Many experiments on various condensing vapors and experimental techniques show disparate temperature dependence to the predictions of the classical nucleation theory (CNT) of Becker and Döring (1935).⁵ Recent refinements of CNT (Refs. 6 and 7) show better agreement with the temperature dependence of experimental data but are still off by several orders of magnitude at absolute scale (e.g., for water, see Ref. 8). Modern approaches such as molecular dynamics (MD) simulation⁹⁻¹² and density functional theory^{13,14} can predict nucleation rates for Lennard-Jones atoms such as noble gases but usually fail for more complex substances, e.g., alcohols and water. Therefore, there exists the need for homogeneous nucleation rate data for substances such as ar-

gon. We designed a cryogenic nucleation pulse chamber to measure homogeneous nucleation rates in supersaturated argon vapor to close the gap between theory and experiment.

Only a few experimental investigations of onsets of homogeneous argon nucleation are reported in literature. First rough data were published by Pierce *et al.*¹⁵ They measured in a supersonic nozzle an approximated region of critical nucleation conditions (onset), i.e., the conditions of vapor pressure and temperature at which nucleation can be observed. Similar measurements using an orifice were reported by Lewis and Williams.¹⁶

The onset is defined dependent on the used experimental setup. First onset measurements with a supersonic nozzle (onset in these experiments corresponds to a nucleation rate of approximately $10^{17} \text{ cm}^{-3} \text{ s}^{-1}$) were performed by Stein¹⁷ and Wu *et al.*¹⁸ Matthew and Steinwandel¹⁹ used a cryogenic shock tube to measure argon nucleation (onset in these experiments corresponds to a nucleation rate of approximately $10^{10} \text{ cm}^{-3} \text{ s}^{-1}$). Their results differ largely from the nozzle experiments. More recent argon onset measurements were reported by Zahoransky *et al.*^{20,21} using a shock tube.

Figure 1 shows the phase diagram of argon including the existing onset data from literature. The unsatisfactory situation is illustrated by the fact that the onset data taken from literature scatter over a wide range of pressure and temperature. The extreme scattering of data points cannot be explained by different onset definitions typical for each experimental method. The necessity of systematic measurements is obvious.

The CNT (Ref. 5) provides predictions in the form of curves of constant nucleation rates of $J_{\text{CNT}} = 10^5 \text{ cm}^{-3} \text{ s}^{-1}$ and $J_{\text{CNT}} = 10^9 \text{ cm}^{-3} \text{ s}^{-1}$ —typical for the measuring window of

^{a)}Present address: Otto-Hahn-Gymnasium, Saaler Mühle 8, D-51429 Bergisch Gladbach, Germany. Electronic mail: fladerer@lo-net.de

^{b)}Author to whom correspondence should be addressed. Electronic mail: rstrey@uni-koeln.de

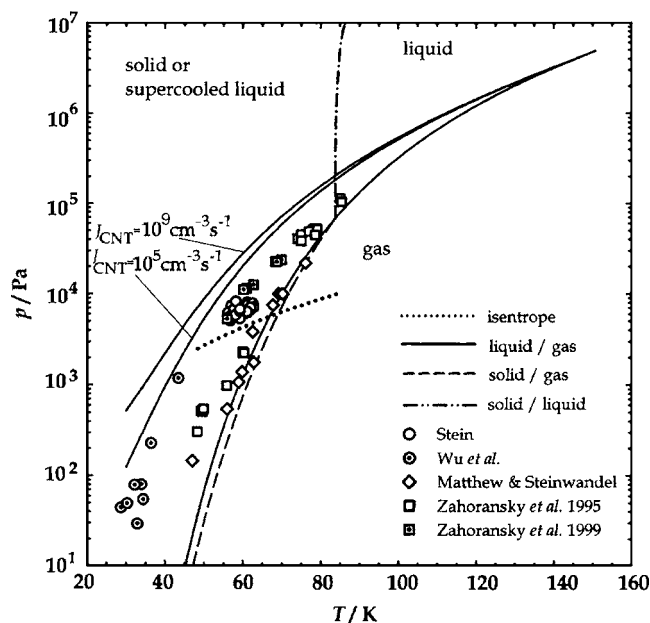


FIG. 1. Phase diagram of argon. The solid line represents the equilibrium vapor pressure $p_{e,l}$ of liquid argon (fit function according to Refs. 22 and 23), while the dashed line is the equilibrium vapor pressure $p_{e,s}$ of solid argon (fit function according to Ref. 24). The other two black lines are calculated according to Becker-Döring theory (CNT) representing a nucleation rates $J_{CNT}=10^9$ and 10^5 $\text{cm}^{-3} \text{s}^{-1}$, respectively, typical for the measuring window of nucleation pulse chambers (Ref. 4). The dotted line is the isentrope symbolizing the change of pressure and temperature for an adiabatic expansion experiment starting at $T_0=84$ K and $p_{v,0}=10$ kPa. Also indicated are some previous nucleation onset data (Refs. 17–21). Onset corresponds to a nucleation rate in the order of 10^{17} $\text{cm}^{-3} \text{s}^{-1}$ in nozzle experiments [Stein (Ref. 17) and Wu *et al.* (Ref. 18)] and of 10^{10} $\text{cm}^{-3} \text{s}^{-1}$ in shock tube experiments [Matthew and Steinwandel (Ref. 19) and Zahoransky *et al.* (Refs. 20 and 21)].

our new chamber (to be described below). They are indicated in Fig. 1. Even though the reported onset data are quite rough, one can already see from this unsatisfactory experimental situation that classical nucleation theory requires much higher vapor pressures for nucleation to occur. In other words, the nucleation rates predicted are much lower compared to the experimental data.

It is also evident that some of the experimental data^{19,20} shown in Fig. 1 are very close to or even located on top of the extrapolated liquid vapor pressure curve. This is a typical signature of heterogeneous nucleation. Postulating the formed clusters to be solid, the original authors were lead to refer their data to the solid vapor pressure curve. However, theoretical arguments and MD simulations clearly indicate that argon clusters of the typical size of a nucleus are still liquid at the given conditions.¹¹ Accordingly, we will advance in Sec. IV a different explanation after we have provided more exact data of the onset of nucleation.

The dotted line in Fig. 1 represents an isentrope resulting from adiabatic expansion with an initial temperature (84 K) and an initial vapor pressure of 10 000 Pa. These are initial conditions typical for the experiment we are going to present in the following.

The paper is organized as follows. First, we describe the design principles and development of a cryogenic nucleation pulse chamber. Then we show the results of the nucleation

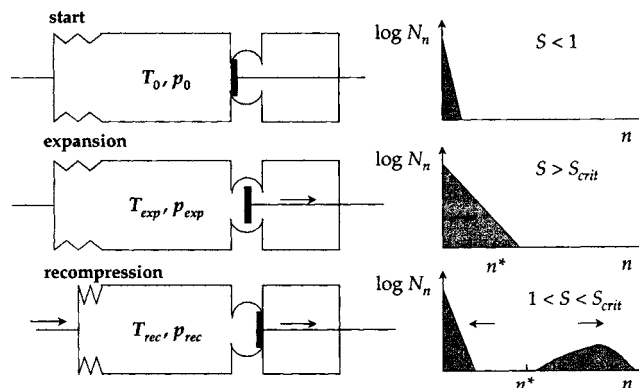


FIG. 2. Schematic illustration of the principle of operation of the cryogenic nucleation pulse chamber.

experiments. We compare the experimental results with classical nucleation theory which dramatically underpredicts the experimental rates. Finally, a comparison of measured droplet growth curves with droplet growth theory is given.

II. EXPERIMENT

Essential for the experimental investigation of homogeneous nucleation is the preparation of a pure supersaturated vapor in the absence of heterogeneous nuclei. This can be achieved by a decrease in temperature in a vapor/carrier gas mixture by means of a rapid expansion. If the design of the measuring chamber allows neglecting heat flux from the wall in the time range of the expansion, the expansions can be treated as adiabatic and the resulting temperature is given by the Poisson equation. The nucleation pulse chamber developed by Strey *et al.*⁴ fulfills these borderline conditions. Hence the design of that chamber was used as model for the cryogenic nucleation pulse chamber presented here. There are some challenging technical problems which had to be solved in constructing a nucleation pulse chamber due to the extreme operating conditions for condensation of noble gases (see Ref. 26). It was decided to study argon condensation which means that the chamber temperature had to be in the 100 K range. So the chamber temperature was set by liquid nitrogen (-196 °C). $\text{N}_2(\text{l})$ was chosen as coolant for cost reasons but it made the use of many common materials impossible. These choices implied that the only reasonable carrier gas was helium. Furthermore, application of the nucleation pulse method demands very fast mechanical response times in the order of milliseconds. This is difficult to realize even at room temperature and much harder at liquid nitrogen conditions. Consequently, a number of innovative features for almost every detail of the cryogenic chamber had to be developed.

A. Principle of operation of the cryogenic pulse chamber

The cryogenic nucleation pulse chamber to be described below in detail is a technical hybrid of the two-piston expansion chamber²⁷ and the single-piston expansion chamber.²⁸ Figure 2 demonstrates the modified function of the expansion principle.

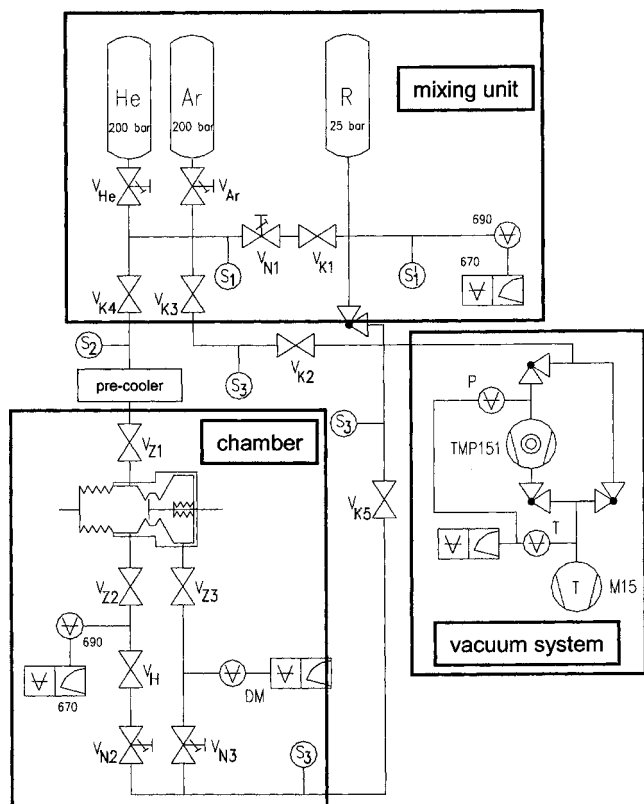


FIG. 3. Block diagram of the experimental arrangement of mixing unit and chamber as well as the vacuum system (schematic). Note that the pre-cooler is held at liquid nitrogen temperature and acts as cold trap for anything but the vapor and the carrier gas.

At the beginning of the experiment the measuring chamber is filled with a vapor/carrier gas mixture (Ar in He) at the pressure p_0 and the temperature T_0 [fixed by $N_2(l)$ to about 83 K]. This mixture is expanded by opening a valve connecting a volume at lower pressure. The pressure drop to p_{exp} results in an adiabatic temperature drop of the gas phase to T_{exp} .

On the right side of Fig. 2 the size distribution N_n of clusters containing n molecules is shown schematically. The temperature drop causes a high supersaturation S_{crit} , leading to a size distribution of clusters that extends to larger sizes. The size of the critical cluster n^* moves from infinity to a value inside the range of the cluster size distribution. Clusters larger than n^* grow spontaneously to macroscopic droplets. This stage of the experiment is the phase of stationary nucleation. It is deliberately terminated by a small recompression of vapor/carrier gas mixture after a few milliseconds. This recompression involves two steps. First the expansion valve is closed to minimize the volume that needs to be compressed. Then the volume is slightly compressed by means of a metallic bellow. Thereby, a small increase in temperature reduces the supersaturation significantly. In this fashion, the formation of new nuclei is quenched but the supersaturation is still high enough so that already formed nuclei can still grow.

The experimental arrangement (Fig. 3) comprises three subunits: vacuum system, vapor/carrier gas mixing unit and nucleation chamber, which are described in detail in the following sections.

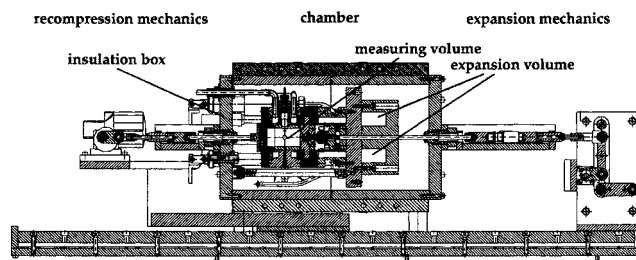


FIG. 4. Technical drawing of the cryogenic nucleation pulse chamber and the insulation box (cross section). Outside the insulation box on the right-hand side is the expansion mechanics located and on the left-hand side the recompression mechanics.

The vapor/carrier gas mixture is prepared in the mixing receptacle R and then piped into the nucleation chamber. The vacuum system can be used for cleaning of the setup with high vacuum and rinsing of the nucleation chamber.

B. The chamber

The cryogenic nucleation pulse chamber is attached to a sidewall of an evacuated insulation box. All pipes and cords are fed through this sidewall. This design allows pulling out the chamber easily from the insulation box for service.

The insulation box and the cryogenic nucleation pulse chamber are thermally disconnected, as shown in a cross section in Fig. 4. Only the chamber itself is cooled with liquid nitrogen supplied from a 0.8 m³ Dewar container (type CT800H, Cryo Diffusion, Lery, France). The insulation box is evacuated (pump: Trivac D4B, Leybold Vakuum GmbH, Cologne, Germany) and the temperature of its sidewalls can be regulated by means of thermostat [type KS20-D, Messgerätewerk (MGW) Lauda—Dr. R. Wobser KG, Lauda-Königshofen, Germany]. The mechanics for the expansion and recompression are mounted outside the insulation box.

The central part of the nucleation pulse chamber is shown in Fig. 5 in a cross section. In the center is the measuring volume (49.51 cm³; inner \varnothing 30 mm); the exchangeable expansion volume (305.18 cm³ in this work) is located on the right-hand side. Measuring and expansion volume are separated by the expansion valve. The expansion shaft is sealed with a bellow against the vacuum of the insulation

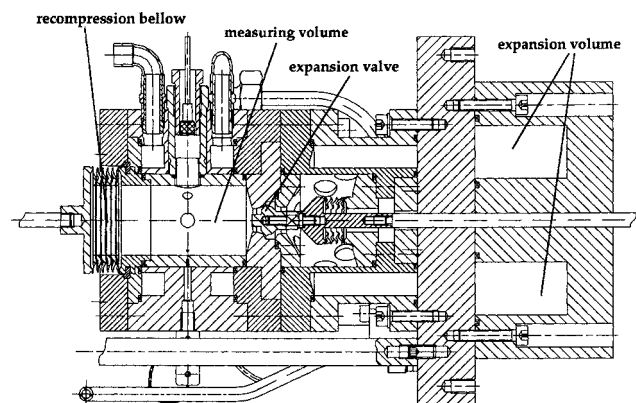


FIG. 5. Blowup of the technical drawing of the center of the cryogenic nucleation pulse chamber.

box. On the left-hand side the metal bellow for the recompression seals against the outside. All movable parts—a source of difficulties to be solved that caused sealing problems at cryogenic conditions—need in total only two seals in the form of stainless steel bellows (COMVAT-Membranbalg; VAT Deutschland GmbH, Grasbrunn, Germany) which are solidly connected to the neighboring components.

The mechanics for the two-step motion of the expansion valve is mounted outside the insulation box. Opening and closing of the valve are controlled by a self-constructed electronic timer.

C. The mixing unit

Argon as condensing vapor and helium as carrier gas are supplied in high purity grade of 6.0 from gas cylinders (Linde AG, Höllriegelskreuth, Germany) to avoid contaminations with other condensable vapors *a priori*. Main possible contamination species are water vapor and—at the cryogenic working conditions—also nitrogen and oxygen. To keep the purity of the supplied gases, special pressure reducing regulators have to be used. For argon the used regulator (type FMD 500-16 E B K6 6, Linde AG, Höllriegelskreuth, Germany) operates in the range of 0.2–3 bars and for helium in the range of 2.5–50 bars (type FMD 500-16 E E K6 6, Linde AG, Höllriegelskreuth, Germany).

The mixing unit is designed for the preparation of vapor/carrier gas up to 2.5 MPa total pressure. The vessel for the mixture is a 10 dm³ gas cylinder made from aluminum (Linde AG, Höllriegelskreuth, Germany) and is mounted in a plastic vessel filled with a water/car-coolant mixture. The temperature of the mixture is controlled by a thermostat (type RCS20-D, Lauda-Dr. R. Wobser GmbH & Co. KG, Lauda-Königshofen) set to 20 °C.

Important for exact measurements is the precise determination of the mixing ratio of vapor and carrier gas during preparation. The pressure in the mixing vessel is measured with a MKS-Baratron pressure sensor (type 690ARCTRB, MKS Instruments Deutschland GmbH, Munich, Germany) in connection with the appropriate display unit (MKS signal conditioner 270D-4).

D. The vacuum system

The used vacuum system Leybold PT 151 Dry (if no other information is given, all parts of the vacuum system were supplied by Leybold Vakuum GmbH, Cologne, Germany) is capable of two modes of application. First, high end vacuum can be achieved for cleaning the mixing vessel (approximately 7×10^{-7} mbar) and the complete setup (approximately 10^{-6} mbar/cleaning mode). Second, the rough vacuum pump allows constant high inlet pressure. This is necessary to rinse the chamber with the vapor/carrier gas mixture between the individual measurements.

The vacuum system consists of an oil-free piston pump (EcoDry M 15) as rough vacuum pump and a turbomolecular pump with DN 100 ISO-K flange (Turbovac 151, type 85631) controlled by an electronic frequency converter (Turbotronik NT 20). Pressure at rough vacuum is measured with Pirani gauge (TTR 90 S) and at high vacuum with a Penning

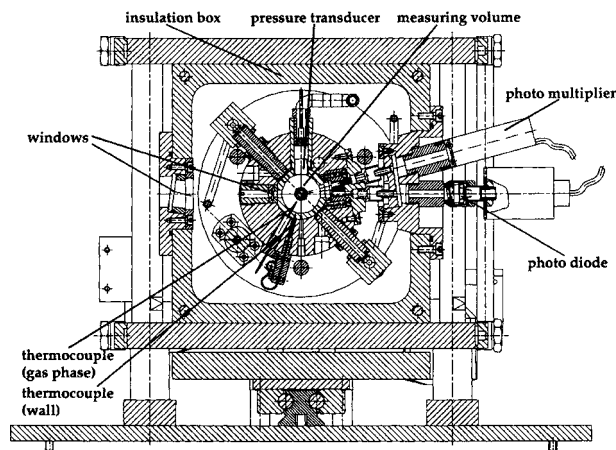


FIG. 6. Cross section of the cryogenic nucleation pulse chamber illustrating the sensor arrangement.

transmitter (PTR 225 S). Data are displayed by the operating and display unit for vacuum transmitters Combivac IT 23.

The vacuum pipes have basically DN 25 ISO-KF flanges. The manually actuated angle valves (type EV 025 SA) are made from aluminum; the angle valve (type EV 025 SX) between the mixing vessel and the vacuum system is made from stainless steel and is laid out for pressures up to 5 MPa. In the measuring mode an additional pipe bypasses the turbomolecular pump.

E. The measuring system

In nucleation experiments the change of pressure and the transmitted and the scattered light have to be measured and recorded as a function of time. For data acquisition a Pentium personal computer (PC) equipped with an analog-to-digital (A/D) converter board (type PCI-9812, ADLink Technology Inc., Taipei, Taiwan) is used.

The change in pressure is detected with a piezo pressure transducer (type 7031, Kistler Instrumente AG, Winterthur, Switzerland). A charge amplifier (type 5011B, Kistler Instrumente AG, Winterthur) converts its signal into voltage.

The droplets formed during an experiment are detected by constant angle Mie scattering (CAMS) at a scattering angle of $\theta = 15^\circ$.²⁹ This technique has proven its reliability in a nucleation pulse chamber for many years.⁴ A polarized HeNe laser (type LK63190P, LG Laser Technologies GmbH, Kleinostheim, Germany) is used as light source. The scattered light is detected with a photomultiplier (type H5784-01, Hamamatsu Photonics Deutschland GmbH, Herrsching, Germany) and the transmitted light with a photodiode (type Centronics OSD50-5T, Laser Components GmbH, Gröbenzell, Germany). Figure 6 shows all sensors in a cross section of the cryogenic nucleation pulse chamber.

The appropriate design of the optics at the cryogenic conditions was a difficult task. The main purpose of the insulation box is to avoid condensation on the optical windows. To this end the insulation box is evacuated and its walls are temperature controlled up to 313 K with a thermostat. To avoid heat conduction between the walls of the insulation box and the nucleation chamber all the optical

guides have to be thermally decoupled. Concurrently, the radiation of parasitic light has to be excluded. The arrangement shown in Fig. 6 ensures these features.

At the beginning of an experiment, the pressures in the measuring and expansion volumes as well as the temperature of the gas phase have to be determined. The pressure in the measuring volume is measured with a MKS-Baratron pressure sensor (type 690A14TRB, MKS Instruments Deutschland GmbH, Munich, Germany) in connection with the appropriate display unit (MKS signal conditioner 270D-4) located outside the insulation box. The pressure in the expansion volume is determined with a pressure sensor (PMP 4010, Druckmesstechnik GmbH, Bad Nauheim, Germany) connected to the vacuum pipe of the expansion volume. The signal of the sensor is converted and displayed in kilopascal units by a digital voltmeter (type 3456A, Hewlett-Packard Corp., Loveland, CO, USA).

The temperature in the gas phase is measured with an open tip type *T* thermocouple (type HTMTIN-M100E-150-IEC, Newport Electronics GmbH, Deckenpfronn, Germany). For control purposes a type *K* thermocouple (type HKMTIN-M100U-100-IEC, Newport Electronics GmbH, Deckenpfronn, Germany) is mounted inside the chamber wall. Chips of type AD595 (Analog Devices Inc., Norwood, MA, USA) compensate and amplify the signals of the thermocouples which are read into the PC and converted into temperature outputs (uncertainty of ± 0.5 K) by calibration functions. As fix points for the calibration functions the boiling points of nitrogen (77.35 K), argon (87.4 K), and oxygen (90.20 K) and the sublimation point of CO₂ (194.70 K) were used. More fixed points at higher temperatures were obtained by an ordinary thermostat.

F. Preparatory steps for the experiments with argon vapor

The cryogenic nucleation pulse chamber allows two types of modes of operation. First, the application of nucleation pulse which is designed to decouple nucleation and droplet growth for the determination of nucleation rates. Second, the vapor-carrier gas mixture may only be expanded to determine that temperature at which nucleation occurs (onset). In the following, the preparations and procedures for such nucleation experiments with argon are described.

Prior to every set of experiments the whole setup is evacuated with the turbomolecular pump (about 10^{-6} mbar). Better vacuum (about 7×10^{-7} mbar) in the mixing vessel is obtained after closing of valves V_K (cf. Fig. 3). After closing the combined high pressure/vacuum angle valve and turning off of the turbomolecular pump a well-defined amount of the vapor (argon) is admitted to the mixing vessel using metering valve V_{N1} . The pressure in the vessel is read after 15 min to let establish equilibrium. The argon in the pipes is pumped out with the rough vacuum pump (valves V_{K2} and V_{K3} have to be opened). After closing V_{K2} and V_{K3} the carrier gas (helium) is added to the mixing vessel using V_{N1} . The total pressure in the mixing vessel is determined after another 15 min.

The cooling of the chamber is started. After reaching an

almost constant temperature below 85 K the piezopressure transducer has to be calibrated. To this end helium is inserted into the chamber controlled with valve V_{He} (V_{K4} and V_{Z1} have to be opened). V_{Z1} is closed and a defined pressure in the measuring volume is set using the needle valve V_{N2} (with the expansion valve closed and V_{Z2} open). Subsequently, V_H is closed and the expansion volume evacuated using V_{Z3} which is also closed afterwards. Before and after opening the expansion valve the pressure is measured with the Baratron of the measuring volume. At the same time, the expansion is recorded with the piezopressure transducer. If both kinds of measurement differ after several expansions by more than 0.2% a new calibration factor is set at the charge amplifier. The new factor is checked by repetition of the calibration procedure. After each cooling of the chamber starting at room temperature, the calibration of the pressure transducer is repeated in order to keep track of irreversible changes.

G. Measurements

At the start of an onset experiment the valves V_{K2} , V_{K4} , V_{Z1} , V_{Z2} , V_{Z3} , V_H , and V_{K5} are open and the cooled chamber is rinsed with the vapor/carrier gas mixture using the rough vacuum pump. The mixture is precooled in a heat exchanger before entering the chamber. The pressure in the chamber is controlled using two valves V_{N1} and V_{N2} . The expansion valve is closed and the expansion volume evacuated. After about 5 min steady-state conditions are established. V_{Z1} is closed and the pressure in the measuring volume is adjusted with V_{N2} . The pressure is read after V_H is closed. After closing V_{Z2} and V_{Z3} the data acquisition is initiated, determining the temperature in the gas phase in the chamber. The expansion valve is opened. The growing droplets are detected by light scattering under an angle of 15° . Simultaneously, pressure and transmitted light are also recorded as a function of time. After the expansion, the expansion valve is closed and the chamber valves V_Z are opened. Before the next experiment the measuring volume is flushed at the desired starting pressure p_0 to clean the chamber.

The nucleation pulse experiments are conducted in a similar way. The main difference is that a preselected pressure has to be set in the expansion volume using V_{N3} . This enables an expansion of the desired depth Δp leading to the conjunct nucleation temperature. Approximately 4 ms after reaching the expansion minimum the recompression is released with the bellow. Simultaneously, the expansion valve is closed again to separate the expansion volume from the measuring volume. The expansion causes the supersaturated vapor to nucleate. The gentle recompression shall quench further nucleation but still allow the already formed droplets to grow. After the experiment all chamber valves are opened and the chamber is flushed for approximately 5 min.

III. RESULTS

A. Nucleation pulse experiments

The nucleation pulse experiment provides as measurable the actual pressure, the intensity of scattered light under an angle of 15° , and the transmitted light as a function of time.

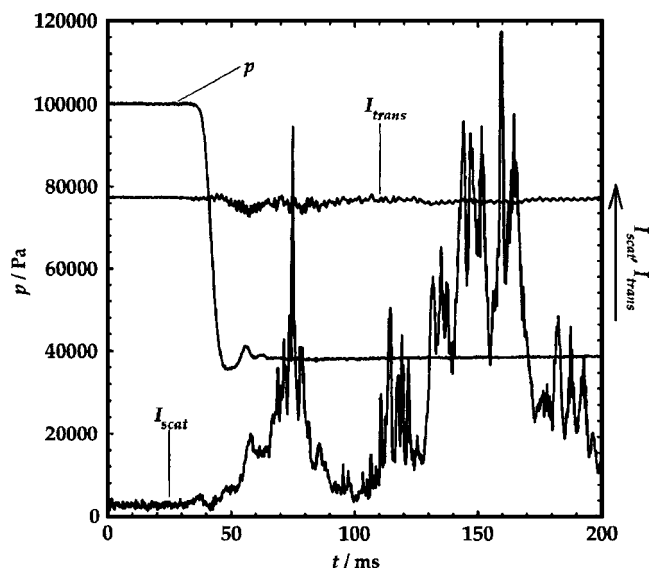


FIG. 7. Time evolution of total pressure p and the intensities of scattered light I_{scat} and transmitted light I_{trans} in a nucleation pulse experiment. Starting conditions: $p_0=100$ kPa, $p_{v,0}=10.05$ kPa, and $T_0=83.70$ K. Conditions at the expansion minimum: $p_{\text{exp}}=35.63$ kPa, $p_{v,\text{exp}}=3.579$ kPa, and $T_{\text{exp}}=55.41$ K.

Figure 7 shows an experimental data set of an experiment with an argon-helium mixture of $\omega_v=10.05\%$. ω_v is the ratio of argon vapor pressure and total pressure.

The initial total pressure of $p_0=100$ kPa drops to the pressure in the expansion minimum p_{exp} . After the time interval Δt_{exp} , the pressure increases to p_{rec} due to the recompression. The temperature at any time of the expansion T_{exp} is calculated by means of the Poisson equation

$$T_{\text{exp}} = T_0 \left(\frac{p_{\text{exp}}}{p_0} \right)^{(\kappa-1)/\kappa}. \quad (1)$$

It should be noted that both argon and helium are noble gases and the ratio of heat capacities κ is exactly 5/3.

Although the sophisticated mechanics provides pressure pulses for the first time in cryogenic systems, nucleation pulse experiments suffered from experimental difficulties and principle limitations. The minimum pulse length Δt_{exp} of approximately 4 ms reached in some experiments is very short for cryogenic systems, especially if compared to the overall duration of the expansion (around 10 ms). This expansion time is, however, comparatively long for characteristic expansion times of approximately 4–5 ms reached in the other nucleation pulse chamber.⁴ However, they are reasonable because of the expansion ratio p_{exp}/p_0 of 0.35, necessary for the observation of argon nucleation, whereas the characteristic expansion ratio of the nucleation pulse chamber⁴ is only 0.7. The smaller pressure drops are feasible because the option of choosing a variable chamber temperature permits experimental starting conditions closer to the equilibrium vapor pressure curve. The chamber temperature in the cryogenic nucleation pulse chamber on the other hand is fixed due to the cooling by liquid nitrogen.

In summary, technically the pulse lengths were hard to handle. But also in technically perfect experiments no reproducible results could be obtained. The reason turned out to

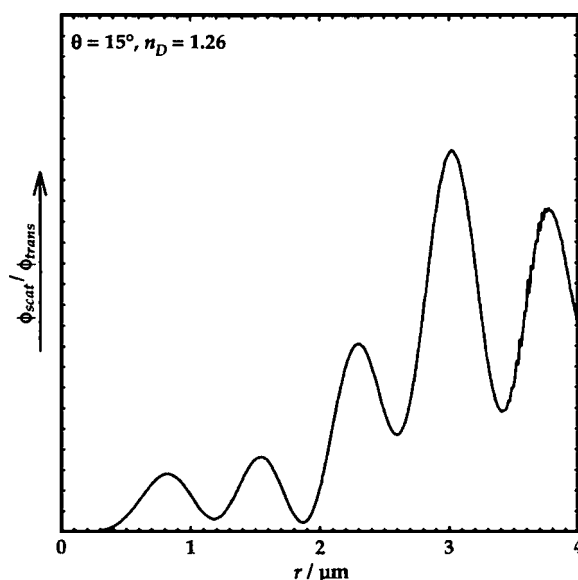


FIG. 8. Theoretical Mie-scattering curve as a function of droplet radius r calculated using Ref. 30. Parameters used: refractive index $n_D=1.26$, scattering angle $\theta=15^\circ$, wavelength $\lambda=632.8$ nm, and 3% polydispersity.

be the fact that the growth of the argon droplets was much faster than anticipated and the growth occurred already during expansion before the pressure minimum was reached. Therefore, only an expansion Δp could be identified at which the scattered light signal reproducibly indicated nucleation. However, the detected light-scattering signal neither could be reproduced in its qualitative shape nor did it agree with the expected structure of the scattering curve calculated from Mie theory (cf. Fig. 8). Also, a variation of ω_v between 1% and 20% could not improve the experimental situation.

Nevertheless, these first nucleation pulse experiments provided us with an interesting insight: Experiments in which no recompression at all was performed also showed nucleation and this in a very reproducible fashion. Therefore, we exploited this aspect systematically and performed experiments which for distinction are called onset experiments.

B. Onset experiments

In the onset experiments the vapor-carrier gas mixture is expanded into vacuum and no recompression is performed. If sufficient supersaturation is reached during expansions the intensity of the scattered light I_{scat} will start to increase due to the growing droplets. If the growth process is so rapid that the moment of nucleation and the time of a discernible increase of the scattering signal are close, the latter point of the scattering signal may be used as sufficiently accurate definition for the onset of nucleation.

In this work onset experiments with four argon concentrations ($\omega_v=19.66\%$, 14.63% , 8.46% , and 4.97%) were conducted. Figure 9 shows a typical onset experiment ($\omega_v=8.46\%$). The onset pressure p_{onset} is determined as the point of time t_{onset} where the scattering signal significantly deviates from the noisy base line. The onset vapor pressure $p_{v,\text{onset}}$ is then calculated as the product of the starting vapor pressure

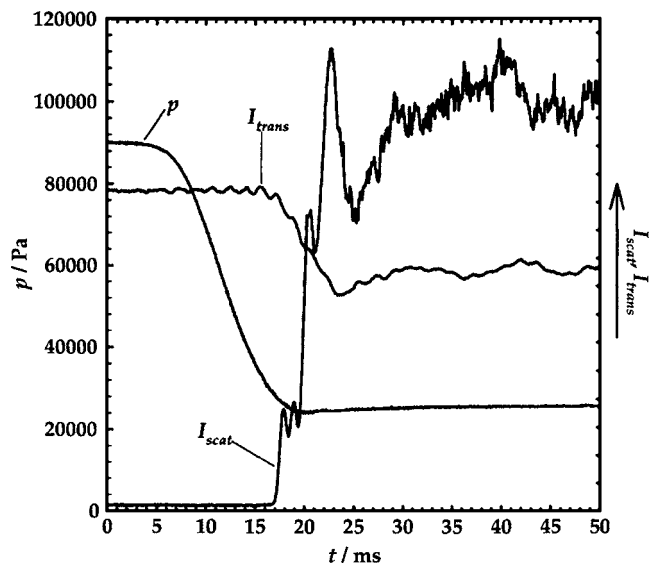


FIG. 9. Time evolution of total pressure p and the intensities of scattered light I_{scat} and transmitted light I_{trans} in an onset experiment at medium starting pressure. Starting conditions: $p_0=90$ kPa, $p_{v,0}=7.615$ kPa, and $T_0=83.55$ K. Onset conditions: $p_{\text{onset}}=29.23$ kPa, $p_{v,\text{onset}}=2.473$ kPa, and $T_{\text{onset}}=53.28$ K.

$p_{v,0}$ and the expansion ratio p_{onset}/p_0 . The respective expansion ratio is used for calculating the onset temperature T_{onset} according to Eq. (1).

The scattering signal sharply deviates from the base line (see Fig. 9). Thus nucleation conditions are determined easily. As a function of time, the scattering signal shows a clear structure of extrema as expected from Mie theory (cf. Fig. 8). The first four maxima can clearly be identified by their height ratios.

A change in initial total pressure p_0 at constant ω_v leads either to an earlier or later occurrence of the onset. In experiments with larger p_0 , onset occurs already in the steep part of the expansion curve and fewer maxima can be observed. This is because of deeper penetration into the supersaturated region. Therefore, higher nucleation rates are achieved leading to a higher number density of droplets. Accordingly, growth is focused on a shorter time interval with faster vapor depletion. Associated is an increase of the gas phase temperature due to latent heat of condensation which in addition more rapidly quenches the growth process at smaller droplet radii. In experiments with lower p_0 , the expansion curve is less steep due to the smaller difference in pressure between the measuring and the expansion volume. Due to the smaller vapor pressure nucleation occurs at lower temperatures, i.e., at the end of the expansion. When nucleation occurs in this flat part of the curve, Mie extrema tend to superimpose. The superimpositions—indicating a higher degree of polydispersity—are stronger the closer to the end of the expansion curve nucleation onset occurs. A reason for this behavior might be longer nucleation times and accordingly smaller number densities.

In summary, the onset experiments can be interpreted as follows: At high starting pressures high nucleation rates and thus high number densities of droplets occur. These systems are self-quenching due to latent heat of condensation and

vapor depletion within a small time interval. Thus, the resulting aerosol is less polydisperse and droplet growth is terminated at smaller droplet radii. At lower starting pressures nucleation rates and the number densities are smaller and the self-quenching effect occurs later and smeared out over a longer time interval. Hence, the time range of nucleation is longer and a more polydisperse aerosol is formed. Both effects lead to a decreasing nucleation rate. Therefore, care must be exercised when comparing the estimated nucleation rate to theory.

IV. DATA ANALYSIS AND DISCUSSION

A. Nucleation behavior of argon

The onset experiments let to 183 data points of vapor pressure and temperature at which signs of nucleation could be determined (see Table I). The data points provide a coherent set of onset data (triangles in Fig. 10), especially if compared to the 73 data points taken from literature.^{17–21} The data cover a temperature range from 49 to 60 K and a pressure range from 800 to 10 000 Pa. The lowest temperature $T_{\text{exp}}=49$ K is the minimal expansion temperature accessible with the present setup and the chamber temperatures of approximately 83.6 K. This minimal temperature is fixed by the maximal expansion ratio limited by both the measuring and expansion volumes. At high temperatures the data measured in this work agree with the newer data measured by Zahoransky *et al.*²¹ (dotted squares). The data at the low temperature end agree with some data points from an earlier work of Zahoransky *et al.*²⁰ (squares). However, other data points from this group are close to the extrapolated vapor pressure curve of liquid argon, which in our opinion indicates heterogeneous nucleation.

B. Estimate of a nucleation rate and comparison with nucleation theory

In nucleation pulse experiments the relative scattering intensity of the first Mie maximum yields the number density of droplets N_d (cf. Ref. 4). The nucleation rate J results from division of N_d by the time range of the expansion minimum Δt_{exp} ,

$$J = \frac{N_d}{\Delta t_{\text{exp}}}. \quad (2)$$

As explained in Sec. III A, the nucleation pulse experiments did not lead to identifiable scattering signals. Thus, N_d could not be determined. Also the pressure pulse did not define the time interval of nucleation. Rather the system quenches itself. The onset experiments were therefore performed as simple expansion and thus the time range of quasi-stationary nucleation conditions Δt_{exp} is not fixed. In addition, the resulting aerosol is not monodisperse and hence N_d cannot be determined exactly. However, by making use of some assumptions resulting from the experience with the nucleation pulse chamber,⁴ a nucleation rate can be estimated from the onset experiments.

In many onset experiments clearly separated Mie extrema can be observed in the scattering signal (e.g., Fig. 9).

TABLE I. Onset data for argon nucleation in helium for four different argon concentrations ω_v . T_0 is the temperature before expansion, p_0 is the total pressure before expansion, $p_{v,0}$ is the vapor pressure before expansion, p_{onset} is the total pressure at onset conditions, $p_{v,\text{onset}}$ is the vapor pressure at onset conditions, and T_{onset} is the temperature pressure at onset conditions.

T_0 (K)	p_0 (Pa)	$p_{v,0}$ (Pa)	p_{onset} (Pa)	$p_{v,\text{onset}}$ (Pa)	T_{onset} (K)
$\omega_v = 19.66\%$					
85.11	120 000	23 587	47 821	9399.6	58.91
84.98	120 000	23 587	47 449	9326.5	58.63
84.67	120 000	23 587	48 689	9570.1	59.02
84.59	120 000	23 587	49 556	9740.7	59.39
84.36	120 000	23 587	50 424	9911.3	59.64
84.17	120 000	23 587	50 424	9911.3	59.50
84.17	120 000	23 587	50 796	9984.4	59.68
84.17	120 000	23 587	49 309	9692.0	58.97
84.04	120 000	23 587	49 928	9813.8	59.18
83.94	110 000	21 622	43 524	8555.2	57.93
83.91	110 000	21 622	43 896	8628.3	58.11
83.91	110 000	21 622	44 516	8750.2	58.43
83.86	110 000	21 622	45 880	9018.3	59.11
83.78	110 000	21 622	44 640	8774.5	58.41
83.76	110 000	21 622	44 020	8652.7	58.07
83.78	110 000	21 622	46 871	9213.2	59.56
83.78	110 000	21 622	45 880	9018.3	59.05
83.76	110 000	21 622	45 384	8920.8	58.78
83.73	110 000	21 622	43 400	8530.8	57.72
83.73	110 000	21 622	44 144	8677.1	58.11
83.73	100 000	19 656	38 979	7661.7	57.42
83.76	100 000	19 656	38 979	7661.7	57.47
83.73	100 000	19 656	39 475	7759.2	57.74
83.73	100 000	19 656	39 971	7856.7	58.03
83.81	100 000	19 656	39 971	7856.7	58.09
83.81	100 000	19 656	40 219	7905.4	58.23
83.81	100 000	19 656	39 475	7759.2	57.80
83.78	100 000	19 656	39 475	7759.2	57.78
83.78	90 000	17 690	34 186	6719.5	56.90
83.76	90 000	17 690	33 566	6597.7	56.47
83.78	90 000	17 690	34 310	6743.9	56.98
83.78	90 000	17 690	33 938	6670.8	56.73
83.76	90 000	17 690	33 814	6646.4	56.63
83.78	90 000	17 690	34 434	6768.3	57.06
83.76	90 000	17 690	33 194	6524.6	56.22
83.65	90 000	17 690	34 310	6743.9	56.89
83.81	90 000	17 690	32 699	6427.1	55.91
83.81	80 000	15 725	29 642	5826.4	56.35
83.78	80 000	15 725	29 890	5875.2	56.52
83.81	80 000	15 725	29 642	5826.4	56.35
83.78	80 000	15 725	29 518	5802.0	56.24
83.81	80 000	15 725	29 270	5753.3	56.07
83.89	80 000	15 725	29 270	5753.3	56.12
83.91	80 000	15 725	29 642	5826.4	56.42
83.94	80 000	15 725	29 022	5704.6	55.97
83.91	80 000	15 725	29 766	5850.8	56.52
$\omega_v = 14.63\%$					
84.80	120 000	17 550	42 737	6250.4	56.11
84.69	120 000	17 550	43 481	6359.1	56.43
84.69	110 000	16 088	40 176	5876.0	56.61
84.56	110 000	16 088	40 672	5948.5	56.80
84.56	110 000	16 088	37 573	5495.2	55.02
84.54	110 000	16 088	37 821	5531.5	55.16
84.38	110 000	16 088	38 193	5585.8	55.27
84.36	110 000	16 088	38 565	5640.2	55.47
84.25	110 000	16 088	40 300	5894.1	56.38
84.30	110 000	16 088	40 548	5930.4	56.55

TABLE I. (Continued.)

T_0 (K)	p_0 (Pa)	$p_{v,0}$ (Pa)	p_{onset} (Pa)	$p_{v,\text{onset}}$ (Pa)	T_{onset} (K)
84.25	100 000	14 625	35 508	5193.0	55.69
84.25	100 000	14 625	35 756	5229.3	55.85
84.28	100 000	14 625	35 384	5174.9	55.64
84.25	100 000	14 625	36 128	5283.6	56.08
84.28	120 000	17 550	45 341	6631.1	57.12
84.28	120 000	17 550	45 465	6649.3	57.18
84.23	120 000	17 550	45 961	6721.8	57.39
84.20	120 000	17 550	45 961	6721.8	57.37
84.23	120 000	17 550	46 705	6830.6	57.76
84.25	120 000	17 550	46 333	6776.2	57.59
84.25	120 000	17 550	46 209	6758.1	57.53
84.25	90 000	13 163	32 203	4709.8	55.86
84.28	90 000	13 163	32 575	4764.2	56.14
84.33	90 000	13 163	31 707	4637.3	55.57
84.33	90 000	13 163	31 831	4655.4	55.66
84.33	90 000	13 163	31 955	4673.5	55.75
84.30	90 000	13 163	31 211	4564.8	55.20
84.28	90 000	13 163	32 203	4709.8	55.88
84.30	90 000	13 163	31 707	4637.3	55.55
84.28	80 000	11 700	27 782	4063.1	55.22
84.25	80 000	11 700	26 666	3899.9	54.30
84.28	80 000	11 700	27 286	3990.6	54.82
84.33	80 000	11 700	27 038	3954.3	54.66
84.30	80 000	11 700	27 038	3954.3	54.64
84.36	80 000	11 700	27 534	4026.8	55.08
84.33	80 000	11 700	27 038	3954.3	54.66
84.30	70 000	10 238	23 237	3398.6	54.25
84.36	70 000	10 238	23 237	3398.6	54.29
84.12	70 000	10 238	22 741	3326.1	53.67
84.33	70 000	10 238	23 733	3471.1	54.73
84.38	70 000	10 238	23 237	3398.6	54.30
84.41	70 000	10 238	22 245	3253.5	53.38
84.36	70 000	10 238	22 245	3253.5	53.35
84.38	70 000	10 238	22 493	3289.8	53.60
$\omega_v = 8.462\%$					
84.23	120 000	10 154	41 746	3532.4	55.21
84.15	120 000	10 154	42 489	3595.3	55.55
84.15	120 000	10 154	41 622	3521.9	55.09
84.02	120 000	10 154	42 242	3574.3	55.34
83.94	120 000	10 154	42 118	3563.8	55.22
83.86	120 000	10 154	39 390	3333.0	53.71
83.83	120 000	10 154	40 754	3448.4	54.42
83.81	120 000	10 154	40 010	3385.5	54.01
83.81	110 000	9 308	35 961	3043.0	53.59
83.78	110 000	9 308	36 209	3063.9	53.72
83.76	110 000	9 308	35 589	3011.5	53.33
83.76	110 000	9 308	35 837	3032.5	53.48
83.73	110 000	9 308	35 589	3011.5	53.32
83.68	110 000	9 308	35 961	3043.0	53.51
83.68	110 000	9 308	35 837	3032.5	53.43
83.68	100 000	8 462	31 416	2658.4	52.66
83.65	100 000	8 462	32 160	2721.4	53.14
83.65	100 000	8 462	31 912	2700.4	52.97
83.63	100 000	8 462	33 896	2868.3	54.25
83.60	100 000	8 462	33 152	2805.3	53.75
83.60	100 000	8 462	33 276	2815.8	53.83
83.57	100 000	8 462	32 656	2763.4	53.41
83.55	100 000	8 462	33 896	2868.3	54.20
83.57	100 000	8 462	34 392	2910.2	54.53
83.55	100 000	8 462	34 020	2878.8	54.28

TABLE I. (Continued.)

T_0 (K)	p_0 (Pa)	$p_{v,0}$ (Pa)	p_{onset} (Pa)	$p_{v,\text{onset}}$ (Pa)	T_{onset} (K)
83.55	90 000	7 615	29 847	2525.4	53.73
83.57	90 000	7 615	29 475	2493.9	53.47
83.52	90 000	7 615	28 979	2452.0	53.08
83.57	90 000	7 615	29 475	2493.9	53.47
83.55	90 000	7 615	29 227	2472.9	53.28
83.52	90 000	7 615	28 483	2410.0	52.71
83.52	90 000	7 615	28 731	2431.0	52.90
83.47	90 000	7 615	29 227	2472.9	53.23
83.52	90 000	7 615	28 979	2452.0	53.08
83.57	80 000	6 769	25 054	2119.9	52.53
83.52	80 000	6 769	25 302	2140.9	52.70
83.52	80 000	6 769	24 682	2088.4	52.18
83.49	80 000	6 769	24 682	2088.4	52.16
83.49	80 000	6 769	24 682	2088.4	52.16
83.47	80 000	6 769	24 558	2077.9	52.04
83.49	80 000	6 769	25 426	2151.4	52.79
83.49	80 000	6 769	25 426	2151.4	52.79
83.55	70 000	5 923	20 881	1766.9	51.50
83.55	70 000	5 923	21 005	1777.4	51.62
83.55	70 000	5 923	21 253	1798.3	51.87
83.57	70 000	5 923	21 005	1777.4	51.63
83.55	70 000	5 923	20 757	1756.4	51.38
			$\omega_v=4.972\%$		
83.52	70 000	5 923	21 501	1819.3	52.09
83.55	70 000	5 923	21 005	1777.4	51.62
83.52	70 000	5 923	20 757	1756.4	51.36
83.55	70 000	5 923	20 757	1756.4	51.38
83.76	110 000	5 469	31 870	1584.5	51.03
83.70	110 000	5 469	32 366	1609.2	51.31
83.69	110 000	5 469	31 994	1590.7	51.07
83.68	110 000	5 469	33 481	1664.6	52.00
83.65	110 000	5 469	34 349	1707.8	52.51
83.57	110 000	5 469	34 473	1713.9	52.54
83.65	110 000	5 469	34 473	1713.9	52.59
83.57	110 000	5 469	34 597	1720.1	52.62
83.57	110 000	5 469	35 093	1744.8	52.92
83.55	110 000	5 469	34 845	1732.4	52.75
83.57	100 000	4 972	30 300	1506.5	51.84
83.55	100 000	4 972	30 176	1500.4	51.74
83.52	100 000	4 972	29 680	1475.7	51.38
83.52	100 000	4 972	29 556	1469.5	51.29
83.49	100 000	4 972	29 309	1457.2	51.10
83.49	100 000	4 972	29 680	1475.7	51.36
83.47	100 000	4 972	29 556	1469.5	51.26
83.47	100 000	4 972	29 432	1463.4	51.18
83.52	90 000	4 475	26 251	1305.3	51.02
83.55	90 000	4 475	25 880	1286.8	50.75
83.52	90 000	4 475	26 004	1293.0	50.83
83.52	90 000	4 475	25 880	1286.8	50.73
83.49	90 000	4 475	25 756	1280.6	50.62
83.52	90 000	4 475	26 128	1299.1	50.93
83.47	90 000	4 475	25 384	1262.1	50.31
83.49	90 000	4 475	25 756	1280.6	50.62
83.47	90 000	4 475	25 756	1280.6	50.60
83.52	80 000	3 978	22 203	1104.0	50.02
83.52	80 000	3 978	22 699	1128.7	50.46
83.52	80 000	3 978	22 451	1116.4	50.24
83.49	80 000	3 978	22 451	1116.4	50.22
83.60	80 000	3 978	22 327	1110.2	50.18
83.65	80 000	3 978	22 451	1116.4	50.32

TABLE I. (Continued.)

T_0 (K)	p_0 (Pa)	$p_{v,0}$ (Pa)	p_{onset} (Pa)	$p_{v,\text{onset}}$ (Pa)	T_{onset} (K)
83.73	70 000	3 481	19 022	945.9	49.72
83.60	70 000	3 481	19 270	958.3	49.90
83.60	70 000	3 481	19 394	964.4	50.03
83.60	70 000	3 481	19 146	952.1	49.77
83.57	70 000	3 481	18 898	939.8	49.50
83.57	60 000	2 983	16 089	799.9	49.36
83.52	60 000	2 983	16 461	818.4	49.79
83.60	60 000	2 983	16 213	806.0	49.53
83.60	60 000	2 983	16 461	818.4	49.83

The ratios of the relative heights of the maxima correspond to a Mie-scattering calculation using the extrapolated refractive index of the liquid phase (Fig. 8). This indicates a self-quenching of the nucleation, as discussed in Sec. III B. Additionally, it can be concluded that the time range of nucleation is shorter than the time difference between the deviation of the scattering signal from its base line ($t_{\text{onset}} = 16.69$ ms for the experiment shown in Fig. 9) and the occurrence of the first Mie maximum because otherwise the Mie extrema would superimpose due to high grade of polydispersity. It is obvious that nucleation begins shortly before the deviation of the scattering signal. Nucleation has to be quenched before the first maximum is reached as otherwise the first and second Mie maxima would not be separated. Hence, the end of the time range of nucleation is approximated by the left inflection point of the first Mie maximum ($t_{\text{end}} = 17.41$ ms for the experiment shown in Fig. 9).

An analysis of the supersaturation as a function of time t for the experiment shown in Fig. 9 allows estimating the start of the time range of nucleation. As supersaturation increases dramatically during the expansion, nucleation onset, indicated by a deviation of the scattering signal from its base

line, takes place at a supersaturation of $S_{\text{onset}} = 11.46$ in this experiment. Few percent lower supersaturation leads to negligible nucleation rates. Thus, the significant supersaturation for nucleation is set arbitrarily to 95% of S_{onset} . This yields the start of the nucleation time range $t_{\text{start}} = 16.43$ ms. The difference between t_{end} and t_{start} can be approximated as Δt to be used in Eq. (3). However, it has to be noted that $\Delta t \approx 1$ ms is not a time range of quasistationary nucleation conditions as in the nucleation pulse experiment but simply a rough estimate of the time range in which nucleation must have taken place.

In addition it is known from the nucleation pulse chamber⁴ that application of CAMS at an angle of 15° allows measurements of droplet concentrations in the range of $5 \times 10^2 < N_d / \text{cm}^{-3} < 5 \times 10^6$. The optics of the cryogenic nucleation pulse chamber is analogous to the nucleation pulse chamber.⁴ Therefore a very similar measuring range is to be expected. Also the scattering signal shows the typical Mie scattering. In the onset experiments at high p_0 the scattering signal is comparable to the calculated Mie-scattering signal. We are safe to conclude that the generated number densities of droplets are in the range of the classic nucleation pulse chamber.⁴ A division of a droplet number density referring to the center of our measuring range $N_d \approx 10^4 \text{ cm}^{-3}$ by the duration of nucleation $\Delta t \approx 1$ ms leads to an estimate of the nucleation rate of $J = 10^7 \text{ cm}^{-3} \text{ s}^{-1}$. The maximum error of this estimate is presumably not more than plus or minus two orders of magnitude. As mentioned before, the data at higher p_0 are the more trustworthy as they refer to a short (natural) nucleation pulse of roughly a millisecond.

Figure 11 shows the predictions of the nucleation rate according to the theories of Becker and Döring⁵ (CNT) and Girshick and Chiu⁶ (GC) as a function of supersaturation at two temperatures representing the upper and lower ends of the measured onset range (52 and 59 K).

These predictions ought to be compared to the estimated nucleation rates. The corresponding supersaturation for these data points is calculated from the onset fit function and the vapor pressure curve for the two temperatures. The error for smaller S results from the difference between S_{onset} and 95% of S_{onset} and for larger S from the difference between the supersaturation at the inflection point of the first Mie maximum and S_{onset} . The error in S decreases if temperature increases. For the experiment shown in Fig. 9 errors of $-\Delta S = 0.58$ and $+\Delta S = 5.7$ result exemplarily.

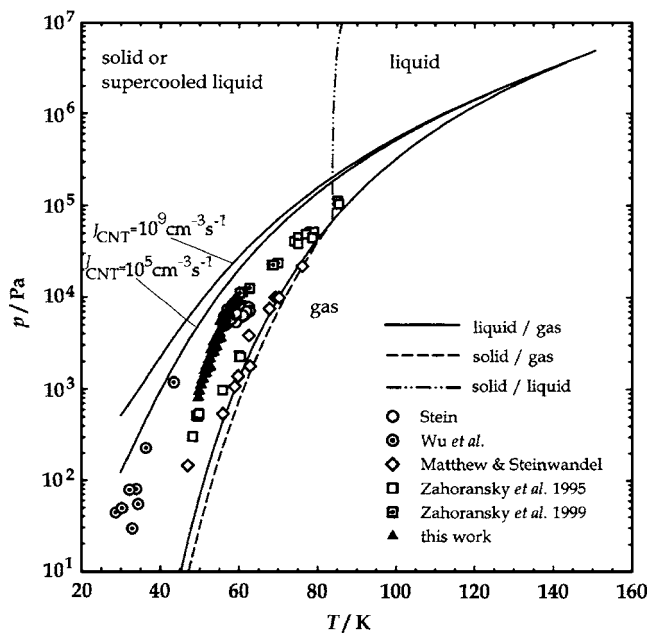


FIG. 10. Same phase diagram as shown in Fig. 1 including the data measured in this work (full triangles).

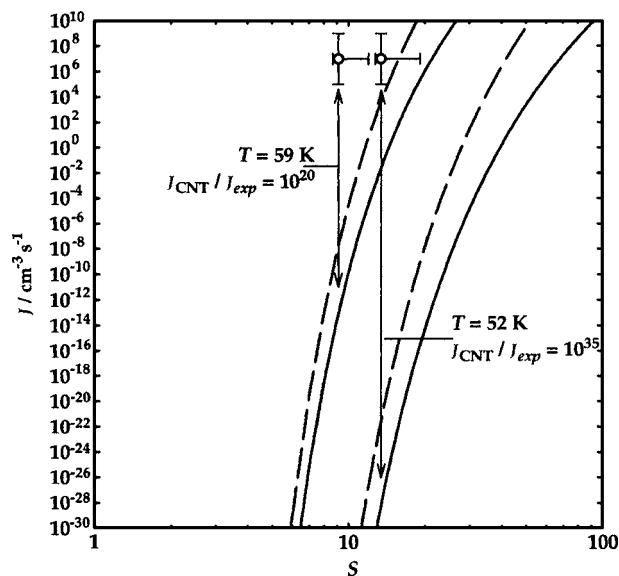


FIG. 11. Comparison of the nucleation rates estimated from the onset data with theoretical predictions according to Becker and Döring (Ref. 5 (CNT/solid line) and Girshick and Chiu (Ref. 6) (dashed line) as a function of supersaturation.

As Fig. 11 illustrates, the error in J of plus or minus two orders of magnitude is negligible compared to the discrepancies of the theoretical predictions. At constant S , the predicted rate according to CNT is 35 orders of magnitude lower at 52 K and 20 orders of magnitude lower at 59 K, respectively. The shift of the GC theory is in the direction of reducing the discrepancy but the nucleation rate of GC is still too low by 28 (at 52 K) and 14 (at 59 K) orders of magnitude. This gap cannot be explained even if the experimental error of plus or minus two orders of magnitude is taken into account.

Density functional calculations by Oxtoby and Evans³¹ predict densities in the core of a critical cluster smaller than the density of the bulk phase. Also the density decreases continuously from the core to the surrounding vapor phase. The density functional approach leads to a nonclassical work of formation of a critical cluster which vanishes at the spinodal in contrast to the classical theory. Hence, there must be a transition region between binodal and spinodal in which the nonclassical work is smaller than the classical work.³² As a result, nonclassical nucleation rates in this region are several orders of magnitude higher than the classical nucleation rates (see also Refs. 33–35). Accordingly, the nonclassical correction predicted by density functional theory tends towards the experimental data of this work.

C. Growth behavior of argon droplets

The scattering signal of the experiment presented in Fig. 9 shows significant Mie maxima as expected from Mie-scattering calculation (cf. Fig. 8). The scattering calculation yields defined radii for each of the extrema, as given in Table II.

Identifying these radii to the times at which the extrema occur in the experiment gives a sequence of $r(t)$ data points forming a droplet growth curve. The time point of onset t_{onset}

TABLE II. Mie extrema and corresponding radii (for $n_D=1.26$, $\theta=15^\circ$).

	Extrema	r (μm)
(1)	Maximum	0.82
	Minimum	1.17
(2)	Maximum	1.54
	Minimum	1.87
(3)	Maximum	2.30
	Minimum	2.60
(4)	Maximum	3.02
	Minimum	3.41
(5)	Maximum	3.77

is approximated as starting time of experimentally observed droplet growth. In the scattering signal of the experiment shown in Fig. 8, four Mie maxima can be identified. This means that the scattering signal is good for seven data points of a growth curve given in Table III.

The droplet growth algorithm of Fladerer and Strey³⁶ based on the droplet growth theory of Fuchs and Sutugin³⁷ allows calculations of droplet growth curves also in highly supersaturated systems.³⁸ It takes into account the change in system, the droplet temperature as well as the vapor depletion. The system conditions at the time t_{onset} are taken as starting conditions. The small change of system temperature due to the continuing expansion after t_{onset} was not included. As the number density of droplets is the only free (but unknown) parameter, several droplet growth curves with various droplet concentrations were calculated.

Figure 12 shows a comparison of the experimental data points according to Table III with calculated growth curves for different number densities. Setting $t_{\text{onset}}=0$ for the comparison is not useful because even the first experimental Mie maximum is broadened due to polydispersity. Hence, the values for the t axis in Table III were recalculated for Fig. 12 in a way that the times, at which the droplet size represented by the first Mie maximum is reached, of both experiment and calculation agree.

All calculated growth curves agree in the early time range and match the experimental data. At later times the calculated growth curves approach a certain limit—the final droplet radii. This limit is smaller the higher the number density of droplets N_d . The growth curve calculated for N_d

TABLE III. Data set of the droplet growth curve of the experiment shown in Fig. 9. The first column contains the times t ($\Delta t = \pm 0.1$ ms) at which the Mie extrema occur in the experiment (with respect to the time of onset) and the second column the corresponding radii r ($\Delta r = \pm 0.1$ μm).

t (ms)	r (μm)
1.18	0.82
1.69	1.17
2.25	1.54
2.66	1.87
3.79	2.30
4.35	2.60
5.99	3.02

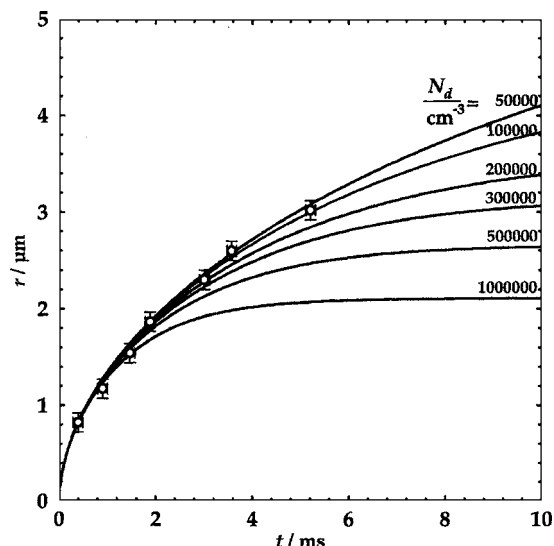


FIG. 12. Growth curve of the experiment shown in Fig. 9 (circles) in comparison to calculated growth curves for various number densities of droplets N_d .

$= 100\,000\text{ cm}^{-3}$ shows best agreement with the experimental data. This number density of droplets is in the range discussed in Sec. IV B.

From knowing the radius as a function of time (e.g. by means of a calculated droplet growth curve) the corresponding Mie-scattering signal as a function of time is accessible, i.e., coupling of the calculated growth curve $r(t)$ with the scattering calculation $I_{\text{scat}}(r)$ allows comparing calculated scattering curve to the experimental scattering signal.

The time dependent scattering curve was calculated using a scattering code of Szymanski³⁰ and the droplet growth algorithm of Fladerer and Strey.³⁶ The degree of polydispersity of the aerosol is free parameter in these calculations. Figure 13 shows a calculation (solid line) with 6% polydispersity in comparison to the experimental scattering signal

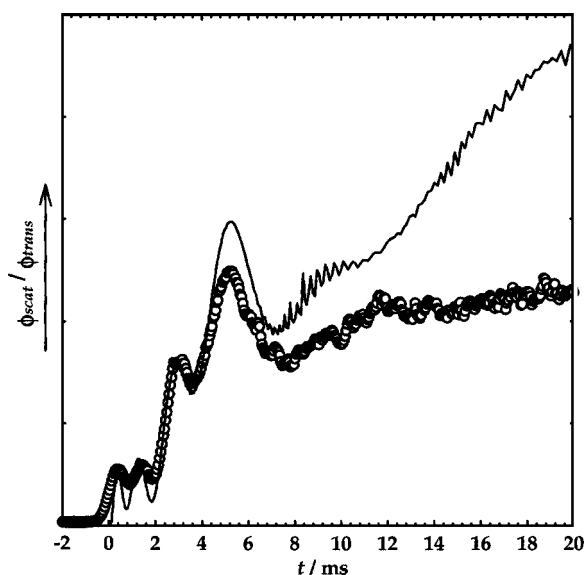


FIG. 13. Comparison of the experimental scattering signal (circles) to a calculated scattering curve (solid line) based on the best growth curve of Fig. 12 ($N_d = 100\,000\text{ cm}^{-3}$; 6% polydispersity).

(circles). The absolute value of the height of first maximum of the calculation was normalized to the experimental value.

As can be seen, not only the times of occurrence of the maxima agree well but also the heights of the first three maxima agree. The fourth maximum in the scattering calculation is slightly higher than the experimental data. A reason for this might be a varying polydispersity as a function of time. This variation may occur due to different fractions of the aerosol moving through the chamber and the scattering volume. After the fourth maximum the superimposition of all higher maxima takes place due to polydispersity resulting in a featureless scattering curve of both experiment and calculation. A variation of the grade of polydispersity in the calculation leads to more visible maxima (2% polydispersity and less) or fewer maxima (10% polydispersity and higher). Therefore, the approximately 6% polydispersity seem to be a reasonable good choice for the generated aerosol. The experimental data shown in Fig. 9 are therefore in every respect qualitatively explained. This fact lends support in the estimate of the time of onset of nucleation as well as of the order magnitude of the number density of droplets estimated.

V. CONCLUSIONS

The analysis of droplet growth in the onset experiments illustrates why the nucleation pulse experiments could not yield interpretable scattering signals and hence did not allow direct measurements of nucleation rates: Droplet growth at nucleation conditions for argon is too fast to decouple nucleation and growth by the pressure pulse. The second Mie maximum representing a droplet size of $1.2\ \mu\text{m}$ occurs less than 2 ms after onset. The presently fastest expansion time of 12 ms and shortest time range of the expansion minimum Δt_{exp} of about 4 ms are still too long and thus prevent decoupling. At this point it is important to realize that calculations of the growth rates (which are almost quantitatively possible as shown above) could not be of guidance in constructing the chamber because the onset of nucleation and herewith temperatures and supersaturations were unknown *a priori*, since existing data were so scattering (cf. Fig. 1). Had one alternatively trusted classical nucleation theory a complete misleading had been the result (as obvious from Figs. 10 and 11). We had to build the chamber, measure and see.

Based on experience gained in the present work, there are several starting points for optimizing the experiments in the cryogenic nucleation pulse chamber in future investigations. Even if the experimental setup is state of the art, by new constructive features an increase of the expansion rate and a shortening the pulse could be achieved. A shortening of the pressure pulse to 1 ms may be hard but not impossible. However, both measures will still not be sufficient to decouple nucleation and growth at the nucleation conditions found in this work, because the growth rate of the droplets is so high. A solution may be experiments at lower temperatures. This would allow experiments with lower vapor pressures. Both lower temperatures and lower vapor pressures will decrease the droplet growth rate. The same effect can also be achieved with higher carrier gas pressures or other carrier gases than helium. The choice of the latter one is

dictated by the immense costs of neon and the risk of cocondensation of the carrier gas. However, faster pressure pulses and slower droplet growth may finally lead to a decoupling of nucleation and growth and hence a direct measurement of nucleation rates of argon.

In the meantime, the easy and routinely feasible application of the onset experiment allows an extension of the current investigation to lower temperatures. Also, other substances than argon condensing at cryogenic conditions may be investigated. For example nitrogen as a simple molecule is a system of theoretical interest which has poorly been studied experimentally.³⁹ A broad and consistent nucleation data set for cryogenic systems is still missing but a first step has been achieved.

ACKNOWLEDGMENTS

The authors are grateful to Eng. H. Metzner and his machine shop team at the Institut für Physikalische Chemie of the Universität zu Köln. Without their expertise, the design and construction of the cryogenic nucleation pulse chamber had not been accomplished. The authors thank Diplom-Ingenieur W. Röhl for design and assembly of electronic equipment, Dr. J. Wölk for overhauling the manuscript, and Dr. K. Iland and Dr. S. Wonzak for fruitful discussions. Financial support of this work by the Deutsche Forschungsgemeinschaft (DFG-Grant Nos. STR311/3-1 and STR311/3-2 “Argon-Keimbildung”) is gratefully acknowledged.

APPENDIX: AUXILIARY DATA

Substances used. Argon (cylinder 1456108) and helium (cylinder 2854689) were supplied in 6.0 qualities in gas cylinders by Linde AG (Höllriegelskreuth, Germany) and used without further purification.

Thermophysical parameters:

Helium

$$M_g = 4.0026 \times 10^{-3} \text{ kg mol}^{-1} \text{ (Ref. 40),}$$

$$C_{p,m,g} = 20.723 \text{ 315 4 J K}^{-1} \text{ mol}^{-1} \text{ (Ref. 41),}$$

χ was calculated according to Eq. (5.62) in Ref. 42, λ_g was calculated according to Eq. (5.56) in Ref. 42,

$$\kappa_g = 5/3.$$

Argon

$$M_v = 39.948 \times 10^{-3} \text{ kg mol}^{-1} \text{ (Ref. 40),}$$

$$C_{p,m,l} = 44.1 \text{ J K}^{-1} \text{ mol}^{-1} \text{ (Ref. 43),}$$

$$T_C = 150.6633 \text{ K (Refs. 44 and 45),}$$

$$p_{v,C} = 4.860 \text{ MPa (Refs. 44 and 46),}$$

$$\rho_C = 13 \text{ 290 mol m}^{-3} = 530.908 \text{ 92 kg m}^{-3} \text{ (Refs. 44 and 45),}$$

$$T_{lp} = 83.804 \text{ K (Ref. 43),}$$

λ_v was calculated according to Eq. (5.55) in Ref. 42,

$$\kappa_v = 5/3.$$

D was calculated according to Eqs. (8.2–44) in Ref. 47.

The liquid density ρ_l is from Ref. 48, the equilibrium vapor pressure for the liquid $p_{e,l}$ from Refs. 44 and 46, the equilibrium vapor pressure of the solid $p_{e,s}$ from Ref. 49, the combined fit for the equilibrium vapor pressure of the liquid and solid $p_{e,l-s}$ from Ref. 50, the surface tension σ from Ref. 51, the heat of vaporization L_l from Ref. 52. The refractive index n_D is calculated from the Lorentz-Lorentz formula (cf. Ref. 53) and Ref. 54 using the appropriate temperature and wavelength.

$$\frac{\rho_l}{\text{kg m}^{-3}} = \frac{M_v}{\text{g mol}^{-1}} \left(\frac{\rho_C}{\text{mol dm}^{-3}} + 24.492 \text{ 48} \left(1 - \frac{T}{T_C} \right)^{0.35} + 8.155 \text{ 083} \left(1 - \frac{T}{T_C} \right) \right),$$

$$p_{e,l} = p_{v,C} \exp \left(\frac{T_C}{T} \left(\begin{array}{l} -5.904 \text{ 188 529} \left(1 - \frac{T}{T_C} \right) + 1.125 \text{ 495 907} \left(1 - \frac{T}{T_C} \right)^{1.5} \\ -0.763 \text{ 257 912 6} \left(1 - \frac{T}{T_C} \right)^3 - 1.697 \text{ 334 376} \left(1 - \frac{T}{T_C} \right)^6 \end{array} \right) \right),$$

$$p_{e,s}/\text{Pa} = \frac{101 \text{ 325}}{760} \left(10^{(7.823 \text{ 114} + (417.0581/T/K))} \left(\frac{T}{K} \right)^{-0.069 \text{ 241 2}} \right),$$

$$p_{e,l-s}/\text{Pa} = ((4.993 \text{ 134 9} \times ((T/K) - 30.179 \text{ 276})^{1.430 \text{ 567 5}} - 1484.9397) \times 10^5,$$

$$\sigma/\text{N m}^{-1} = 0.037 \text{ 78} \times (1 - (T/T_C))^{1.277},$$

$$L_l/\text{J kg}^{-1} = 4.184 \times (1808.612 \text{ 27} + 1.076 \text{ 293 16} \times (T/K) - 0.046 \text{ 477 545 3} \times (T/K)^2) / (M_l/(\text{kg mol}^{-1})),$$

$$n_D = 1.2321.$$

- ¹C. T. R. Wilson, *Philos. Trans. R. Soc. London, Ser. A* **189**, 265 (1897).
- ²R. H. Heist and H. J. He, *J. Phys. Chem. Ref. Data* **23**, 781 (1994).
- ³E. F. Allard and J. L. Kassner, *J. Chem. Phys.* **42**, 1401 (1965).
- ⁴R. Strey, P. E. Wagner, and Y. Viisanen, *J. Phys. Chem.* **98**, 7748 (1994).
- ⁵R. Becker and W. Döring, *Ann. Phys. (Leipzig)* **24**, 719 (1935).
- ⁶S. L. Girshick and C.-P. Chiu, *J. Chem. Phys.* **93**, 1273 (1990).
- ⁷H. Reiss, W. K. Kegel, and J. L. Katz, *J. Phys. Chem. A* **102**, 8548 (1998).
- ⁸J. Wölk and R. Strey, *J. Phys. Chem. B* **105**, 11683 (2001).
- ⁹P. Rein ten Wolde and D. Frenkel, *J. Chem. Phys.* **109**, 9901 (1998).
- ¹⁰K. Laasonen, S. Wonczak, R. Strey, and A. Laaksonen, *J. Chem. Phys.* **113**, 9741 (2000).
- ¹¹S. Wonczak, Ph.D. thesis, Universität zu Köln, 2001.
- ¹²S. Toxvaerd, *J. Chem. Phys.* **115**, 8913 (2001).
- ¹³X. C. Zeng and D. W. Oxtoby, *J. Chem. Phys.* **94**, 4472 (1991).
- ¹⁴V. Talanquer and D. W. Oxtoby, *J. Chem. Phys.* **100**, 5190 (1994).
- ¹⁵T. Pierce, P. M. Sherman, and D. D. McBride, *Astronaut. Acta* **16**, 1 (1971).
- ¹⁶J. W. L. Lewis and W. D. Williams, NTIS Report No. AD782445, 1974.
- ¹⁷G. D. Stein, NTIS Report No. ADA007357, 1974.
- ¹⁸B. J. C. Wu, P. P. Wegener, and G. D. Stein, *J. Chem. Phys.* **69**, 1776 (1978).
- ¹⁹M. W. Matthew and J. Steinwandel, *J. Aerosol Sci.* **14**, 755 (1983).
- ²⁰R. A. Zahoransky, J. Höschele, and J. Steinwandel, *J. Chem. Phys.* **103**, 9038 (1995).
- ²¹R. A. Zahoransky, J. Höschele, and J. Steinwandel, *J. Chem. Phys.* **110**, 8842 (1999).
- ²²R. B. Stewart and T. Jacobsen, *J. Phys. Chem. Ref. Data* **18**, 639 (1989).
- ²³W. Wagner, *Cryogenics* **13**, 470 (1973).
- ²⁴H. H. Chen, C. C. Lim, and R. A. Aziz, *J. Chem. Thermodyn.* **10**, 649 (1978).
- ²⁵W. H. Hardy, R. K. Crawford, and W. B. Daniels, *J. Chem. Phys.* **54**, 1005 (1971).
- ²⁶A. Fladerer, Ph.D. thesis, Universität zu Köln, 2002; <http://kups.ub.uni-koeln.de/volltexte/2003/465/>
- ²⁷P. E. Wagner and R. Strey, *J. Phys. Chem.* **85**, 2694 (1981).
- ²⁸K. Iland, J. Wölk, and R. Strey, *J. Aerosol Sci.* **32**, S105 (2001).
- ²⁹P. E. Wagner, *J. Colloid Interface Sci.* **105**, 456 (1985).
- ³⁰W. Szymanski, *LEAD. FOR. FORTRAN-Programm zur Berechnung von Streulichtintensitäten*, Universität Wien, 1980; Basic transcription: S. Wonczak, Universität zu Köln, 1998.
- ³¹D. W. Oxtoby and R. Evans, *J. Chem. Phys.* **89**, 7521 (1988).
- ³²J. W. P. Schmelzer, I. Gutzow, and J. Schmelzer, *J. Colloid Interface Sci.* **178**, 657 (1996).
- ³³R. Strey, P. E. Wagner, and T. Schmeling, *J. Chem. Phys.* **84**, 2325 (1986).
- ³⁴H. Uchtmann, S. Yu. Kazitsyna, F. Hensel, V. Zdimal, B. Triska, and J. Smolík, *J. Phys. Chem. B* **105**, 11754 (2001).
- ³⁵M. Rusyniak, V. Abdelsayed, J. Campbell, and M. S. El-Shall, *J. Phys. Chem. B* **105**, 11866 (2001).
- ³⁶A. Fladerer and R. Strey, *Atmos. Res.* **65**, 161 (2003); See also A. Fladerer, diploma thesis, Universität zu Köln, 1998; <http://kups.ub.uni-koeln.de/volltexte/2006/1641/>
- ³⁷N. A. Fuchs and A. G. Sutugin, *Highly Dispersed Aerosols* (Ann Arbor Science, Ann Arbor, MI, 1970).
- ³⁸A. Fladerer, M. Kulmala, and R. Strey, *J. Aerosol Sci.* **33**, 391 (2002).
- ³⁹R. A. Zahoransky, *Z. Flugwiss. Weltraumforsch.* **10**, 34 (1986).
- ⁴⁰A. F. Holleman, E. Wiberg, and N. Wiberg, *Lehrbuch der Anorganischen Chemie*, 91st–100th ed. (Walter de Gruyter, Berlin, 1985).
- ⁴¹*Gmelins Handbuch der Anorganischen Chemie*, 8th ed. (Verlag Chemie, Leipzig, 1926), System-Nummer 1 (Edelgase), p. 65.
- ⁴²P. E. Wagner, in *Topics in Current Physics, Aerosol Microphysics Vol. II*, edited by W. H. Marlow (Springer-Verlag, Berlin, 1982), Vol. 29, p. 129.
- ⁴³C. Gladun, *Cryogenics* **11**, 205 (1971).
- ⁴⁴R. B. Stewart and T. Jacobsen, *J. Phys. Chem. Ref. Data* **18**, 639 (1989).
- ⁴⁵A. V. Voronel, V. G. Gorbunova, V. A. Smirnov, N. G. Shmakov, and V. V. Shchekochikhina, *Sov. Phys. JETP* **36**, 505 (1973).
- ⁴⁶W. Wagner, *Cryogenics* **13**, 470 (1973).
- ⁴⁷J. O. Hirschfelder, C. F. Curtiss, and R. B. Bird, *Molecular Theory of Gases and Liquids*, 2nd ed. (Wiley, New York, 1965), p. 600.
- ⁴⁸W. M. Haynes, *Cryogenics* **18**, 621 (1978).
- ⁴⁹H. H. Chen, C. C. Lim, and R. A. Aziz, *J. Chem. Thermodyn.* **10**, 649 (1978).
- ⁵⁰W. H. Hardy, R. K. Crawford, and W. B. Daniels, *J. Chem. Phys.* **54**, 1005 (1971).
- ⁵¹F. B. Sprow and J. M. Prausnitz, *Trans. Faraday Soc.* **62**, 1097 (1966).
- ⁵²G. N. Brown and W. T. Ziegler, *Adv. Cryog. Eng.* **25**, 662 (1980).
- ⁵³P. W. Atkins, *Physikalische Chemie*, 1st ed. (VCH, Weinheim, 1990).
- ⁵⁴A. C. Sinnock and B. L. Smith, *Phys. Rev.* **181**, 1297 (1969).